JOURNAL OF COMPUTATIONAL PHYSICS 17, 160–180 (1975)

Numerical Solutions for Supersonic Corner Flow

V. SHANKAR AND D. ANDERSON

Department of Aerospace Engineering and Engineering Research Institute, Iowa State University, Ames, Iowa 50010

AND

P. KUTLER

Computational Fluid Dynamics Branch, NASA Ames Research Center, Mt. View, California 94040

Received August 8, 1974; revised October 9, 1974

Analytical solutions for inviscid supersonic corner flows are virtually nonexistent due to the complexity of the interference geometry. In view of this, numerical solutions for swept-compressive and swept-expansive corner flows are obtained. The governing equations are written in strong conservation-law form and are solved iteratively in nonorthogonal conical coordinates by use of a second-order, shock-capturing, finite-difference technique. The computed wave structure and surface pressure distributions are compared with high Reynolds number ($Re > 3 \times 10^6$) experimental data and show very good agreement. The results clearly show that supersonic corner flow at reasonably high Reynolds numbers including the effect of sweep is dominated by the inviscid field.

INTRODUCTION

The three-dimensional supersonic flow produced by two intersecting wedges has received considerable study in the past decade. This type of flow occurs in supersonic inlet systems, at wing–body juctures and numerous other places where at least two surfaces intersect. The interference flow produced near these intersections usually results in significant rises in heat transfer and skin friction.

Charwat and Redekopp [1] conducted experiments on the corner flow produced by two intersecting 12.2° wedges at a free-stream Mach No. of 3.17. The resulting wave structure showed that the two wedge shocks do not intersect but are joined by a third corner shock. Korkegi [2] more recently predicted that the most general case consists of a corner shock joining the two wedge shocks. Watson and Weinstein [3] made measurements on a similar configuration at Mach 20. Measurements of surface heating rates, pressure, and the viscous–inviscid interaction were made by Cresci [4] and Stainback [5, 6] for hypersonic flows. In more recent

publications, experimental data were obtained for the corner flow problem by West and Korkegi [7] at Mach 3 for wedge angles of 9.5° and very high Reynold's numbers (0.4 to 60 $\times$ 10^6). This high Reynold's number data produced an improved picture of the inviscid wave structure in the corner because the flow was turbulent. The flow structure predicted by West and Korkegi (Fig. 1) consists of a corner shock joining the two wedge shocks with embedded shocks emanating from the triple points and impinging on the wedge surfaces. In addition, two contact or slip surfaces join the triple points with the axial corner. These slip surfaces are slightly curved and asymptotically approach the bisector near the axial corner rather than being straight as indicated by Charwat and Redekopp.

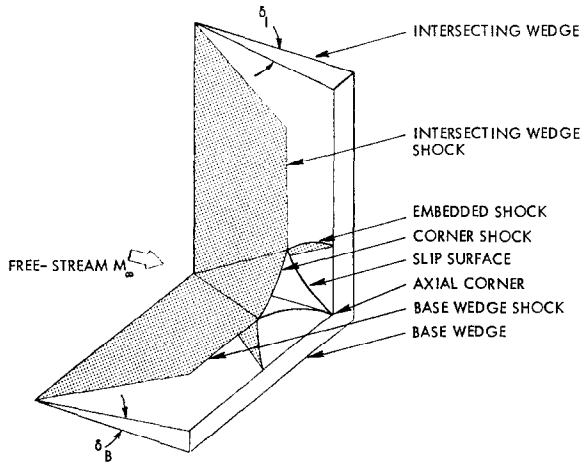

FIG. 1. Wave structure in the compression–compression corner.

Due to the complex interference flow produced in the axial corner, development of analytical models has been slow. Most early models of the corner flow problem were either incorrect or were based upon linear theory and the resulting solutions were inadequate [8, 9]. Wallace and Clarke [8] developed a second-order iterative solution for corner flow. Using this method, discontinuities appeared in the potential functions across plane shock waves. Shortcomings of this theory also produced singularities in the velocity at the intersection of these shocks with the wedge surfaces. Goebel [9] developed an analytical model based upon experimental observations which has been used. However, a unique solution for the embedded shocks is not assured using Goebel's results. Korkegi [10] states that "there exists no adequate method of predicting even the inviscid flow structure." Kutler [11] has recently developed a numerical technique for solving the inviscid unswept compressive–compressive corner flow problem.

When the corner geometry is immersed in an inviscid supersonic free stream, the resulting flow field is conical because of the absence of a characteristic length along rays emanating from the apex. This requires that the fluid variables be constant along each of these rays. The steady gas dynamic equations are hyperbolic with respect to integration in the radial direction. If the equations are integrated along the conical rays starting from some initial surface, the results should asymptotically approach the conical solution. This approach is used herein to obtain a solution to the corner flow problem.

The resulting interference flow in the corner may be classified as (i) fully compressive, (ii) "mixed," i.e., one wedge producing compression and the other expansion, and (iii) fully expansive, according to corner geometry. The aforementioned experimental and theoretical investigators have confined their studies to the fundamental, right-angled, unswept, compressive corner configuration of class (i), where both the intersecting and base wedges produce planar shocks. Study of "mixed" corner flows and swept corner flows is important in view of present-day flight configurations which have components that are either swept or form an expansive surface. Nangia [12] has more recently obtained experimental solutions for the three types of corner flows at various Mach numbers with particular emphasis on Mach 2 testing. His study was conducted for considerably higher Reynolds numbers than was the study of Charwat and Redekopp. The boundary layer on the model was made artificially turbulent to minimize boundary layer effects.

In the present study, numerical solutions are obtained and compared with the experimental results of Charwat and Redekopp for (1) $M_\infty = 3.17$, $\delta_B = 12.2°$, $\delta_I = 12.2°$, and $\Lambda = 0°$; and Nangia for (2) $M_\infty = 2$, $\delta_B = 5°$, $\delta_I = 7.5°$, $\Lambda = 0°$; (3) $M_\infty = 2$, $\delta_B = -5°$, $\delta_I = 7.5°$, $\Lambda = 0°$; (4) $M_\infty = 2$, $\delta_B = 5°$, $\delta_I = 7.5°$, $\Lambda = 30°$; and (5) $M_\infty = 2$, $\delta_B = -5°$, $\delta_I = 7.5°$, $\Lambda = 30°$.

II. Governing Partial-Differential Equations

The geometry for the swept compression–compression ($\delta_B > 0$, $\delta_I > 0$) and swept expansion–compression corner arrangements is shown in Figs. 2 and 3. The origin is at the intersection of the two leading edges with x measured along the free-stream direction.

The governing partial-differential equations (continuity, x, y, and z momentum) in a Cartesian coordinate system for a steady, inviscid, nonheatconducting and adiabatic flow are given by

$$(\partial E/\partial x) + (\partial F/\partial y) + (\partial G/\partial z) = 0, \tag{1}$$

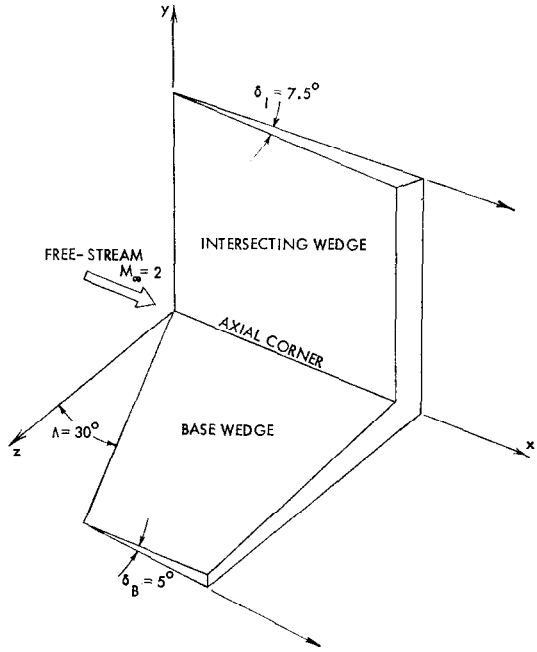

FIG. 2. Geometry for a swept compressive–compressive 90° corner arrangement.

where

$$E = \begin{vmatrix} \rho u \\ kp + \rho u^2 \\ \rho uv \\ \rho uw \end{vmatrix}; \quad F = \begin{vmatrix} \rho v \\ \rho uv \\ kp + \rho v^2 \\ \rho vw \end{vmatrix}; \quad G = \begin{vmatrix} \rho w \\ \rho uw \\ \rho vw \\ kp + \rho w^2 \end{vmatrix},$$

where $k = (\gamma - 1)/2\gamma$ and γ is the specific heat ratio of the gas.

In (1), pressure and density are made dimensionless with respect to the free-stream stagnation conditions and velocity with respect to the maximum adiabatic velocity. In order to alleviate the numerical difficulties in assigning boundary conditions (it is desirable to choose a coordinate system in which the body coincides with one of the coordinate directions), the governing equations in Cartesian space are transformed into nonorthogonal, conical coordinates

$$\begin{aligned} \zeta &= x, \\ \eta &= y/(x - z \tan \Lambda), \\ \xi &= z/x, \end{aligned} \tag{2}$$

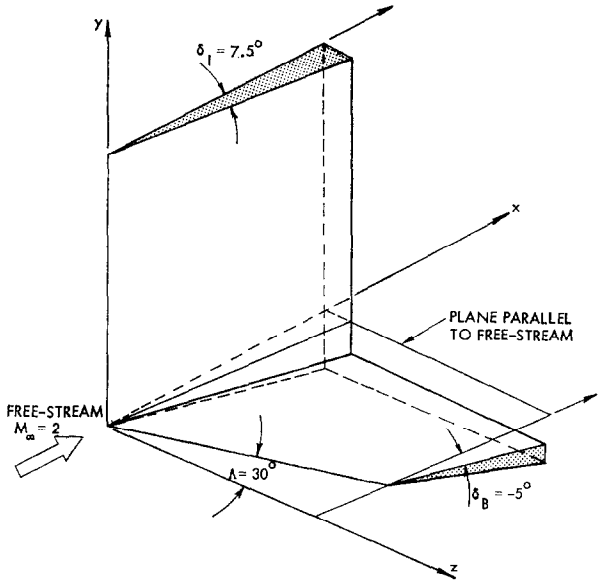

FIG. 3. Geometry for a swept compressive–expansive 90° corner arrangement.

and rearranged in strong conservation-law form to yield the following dimensionless equation.

$$(\partial \bar{E}/\partial \zeta) + (\partial \bar{F}/\partial \eta) + (\partial \bar{G}/\partial \xi) = 0, \tag{3}$$

where

$$\begin{aligned} \bar{E} &= r\zeta E, \\ \bar{F} &= \zeta(F - \eta E) + \zeta \eta G \tan \Lambda, \\ \bar{G} &= r(G - \xi E), \\ r &= \zeta(1 - \xi \tan \Lambda). \end{aligned}$$

The dimensionless form of the integrated energy equation is

$$p = \rho(1 - u^2 - v^2 - w^2). \tag{4}$$

Equations (3) and (4) form a system of five equations with five unknowns p, ρ, u, v, and w.

Equation (3) is hyperbolic with respect to the ζ coordinate, and the problem is a well-posed initial-value problem. Solutions can be obtained by numerically integrating the equation with respect to the hyperbolic direction.

III. Boundary and Initial Conditions

The base and intersecting wedge surfaces are defined by a constant η and a constant ξ, respectively. The boundary condition at the surface of each wedge requires that the flow be tangent to it. This yields the following boundary conditions.

$$\begin{aligned} v &= u \tan \delta_B - w \tan \Lambda \tan \delta_B, \qquad \text{at the base wedge surface,} \\ w &= u \tan \delta_I, \qquad \text{at the intersecting wedge surface.} \end{aligned} \tag{5}$$

At the axial corner both of Eqs. (5) are used as boundary conditions.

Figure 4 shows the mesh system in the physical corner region. The intersection

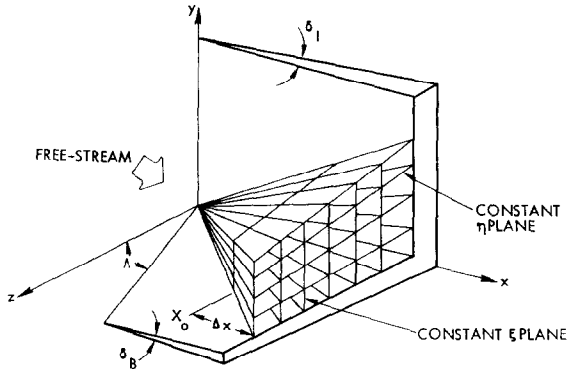

FIG. 4. Mesh system in the physical corner region for a swept compression–compression corner.

of constant η and constant ξ planes yields a rectangular computational region with grid points lying on conical rays. The size of the rectangular computational region is chosen such that it encompasses the wave structure in the corner. In Figs. 5 and 6, $i = 1$ corresponds to the base wedge surface, and $j = 1$ corresponds to the intersecting wedge surface. The upper boundaries in the η and ξ directions are $i_{\max}$ and $j_{\max}$, respectively, and are chosen to fall in a region of known flow properties.

Initial starting solutions are specified at each of the grid points in the computational plane. All interior points ($1 \leqslant j \leqslant j_{\max} - 1$ and $1 \leqslant i \leqslant i_{\max} - 1$) are assigned values of the free-stream conditions given by

$$\begin{aligned} p_\infty &= [1 + (\gamma - 1)\, M_\infty^2/2]^{-\gamma/\gamma-1}, \\ \rho_\infty &= [1 + (\gamma - 1)\, M_\infty^2/2]^{-1/\gamma-1}, \\ u_\infty &= \left[\frac{(\gamma - 1)\, M_\infty^2/2}{1 + (\gamma - 1)\, M_\infty^2/2}\right]^{1/2}, \\ v_\infty &= 0, \\ w_\infty &= 0. \end{aligned} \tag{6}$$

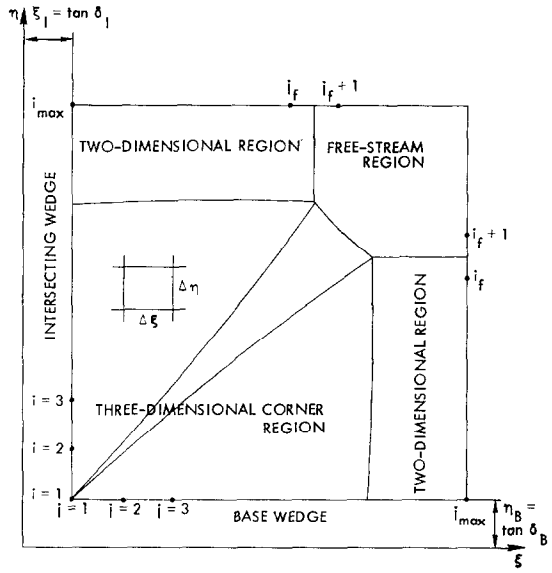

FIG. 5. Rectangular computational region encompassing the shock structure in the compression–compression corner.

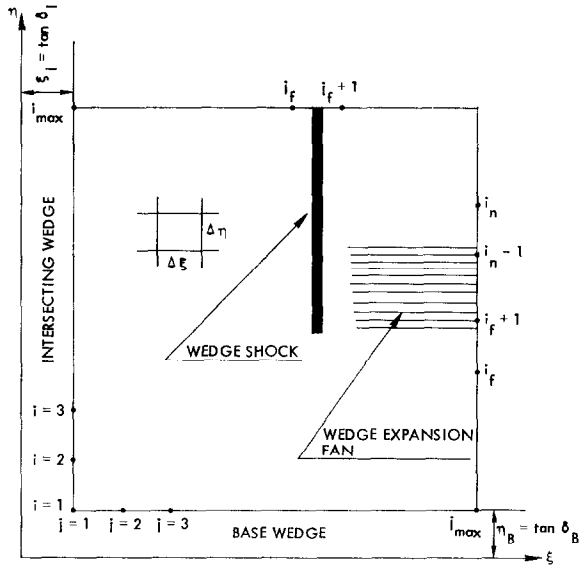

FIG. 6. Rectangular computational region for an expansion–compression corner.

Knowing the free-stream conditions and the wedge angles δ_B and δ_I, the exact two-dimensional conditions can be calculated. In Fig. 5, along the outer boundaries $i_{\max}$ and $j_{\max}$ exact two-dimensional solutions are specified at points $1 \leqslant i \leqslant i_f$ and $1 \leqslant j \leqslant j_f$, with the free-stream conditions applied at points $i_f + 1 \leqslant i \leqslant i_{\max}$ and $j_f + 1 \leqslant j \leqslant j_{\max}$. In the case of expansion–compression corner flow, specification of two-dimensional conditions along the outer boundary $j_{\max}$ (Fig. 6) requires the calculation of flow variables within the expansion fan (points $i_f + 1 \leqslant i \leqslant i_n - 1$). Since the location of the wedge shock and the wedge expansion fan are known, i_f and j_f are chosen such that the computational mesh is created to position them exactly halfway between two adjacent grid points. This determines the mesh intervals $\Delta\eta$ and $\Delta\xi$. The conditions along the outer boundary $i_{\max}$ and $j_{\max}$ are held fixed during the entire computation.

When the expansive base wedge is swept, the two-dimensional solutions cannot be calculated in a closed form. Therefore, free-stream conditions are specified along $j_{\max}$ for $1 \leqslant i \leqslant i_{\max}$ as an initial solution. At the end of each iteration cycle the flow variables along $j_{\max}$ are set equal to the flow variables along $(j_{\max} - 1)$ to satisfy the zero gradient condition in the two-dimensional region.

IV. Integration Procedure

Since the multishocked flow field is "captured" by the difference algorithm, the choice of the finite-difference scheme to be used is of importance. MacCormack's [13] second-order, predictor–corrector scheme, probably the most efficient algorithm to use in a shock-capturing technique, was chosen. For shocks which propagate upwards from the body, use of a forward-predictor and backward-corrector algorithm yields excellent results.

Applied to Eq. (3), it takes the form:

$$\tilde{\bar{E}}^{n+1}_{i,j} = [\bar{E}^n_{i,j} - (\Delta\zeta/\Delta\eta)(\bar{F}^n_{i+1,j} - \bar{F}^n_{i,j}) - (\Delta\zeta/\Delta\xi)(\bar{G}^n_{i,j+1} - \bar{G}^n_{i,j})], \tag{7a}$$

$$\bar{E}^{n+1}_{i,j} = \tfrac{1}{2}[\bar{E}^n_{i,j} + \tilde{\bar{E}}^{n+1}_{i,j} - (\Delta\zeta/\Delta\eta)(\tilde{\bar{F}}^{n+1}_{i,j} - \tilde{\bar{F}}^{n+1}_{i-1,j}) - (\Delta\zeta/\Delta\xi)(\tilde{\bar{G}}^{n+1}_{i,j} - \tilde{\bar{G}}^{n+1}_{i,j-1})], \tag{7b}$$

where subscripts i, j refer to mesh points, the superscript n refers to integration steps in the ζ direction and the circumflex $\sim$ refers to predictor values. This scheme is applied at the grid points bounded by $2 \leqslant j \leqslant j_{\max} - 1$ and $2 \leqslant i \leqslant i_{\max} - 1$. At the surface of each wedge ($j = 1$, $i = 1$), the backward corrector (Eq. (7b)) is not applicable as no backward grid points are available. Thus, a one-sided differencing scheme is used at the body by modifying the corrector (Eq. (7b)) as follows.

$$\bar{E}^{n+1}_{i,j} = \tfrac{1}{2}[\bar{E}^n_{i,j} + \tilde{\bar{E}}^{n+1}_{i,j} - (\Delta\zeta/\Delta\eta)(\tilde{\bar{F}}^{n+1}_{i+1,j} - \tilde{\bar{F}}^{n+1}_{i,j}) - (\Delta\zeta/\Delta\xi)(\tilde{\bar{G}}^{n+1}_{i,j} - \tilde{\bar{G}}^{n+1}_{i,j-1})] \tag{7c}$$

for the base wedge grid points and

$$\bar{E}_{i,j}^{n+1} = \tfrac{1}{2}[\bar{E}_{i,j}^{n} + \tilde{\bar{E}}_{i,j}^{n+1} - (\Delta\zeta/\Delta\eta)(\tilde{\bar{F}}_{i,j}^{n+1} - \tilde{\bar{F}}_{i-1,j}^{n+1}) - (\Delta\zeta/\Delta\xi)(\tilde{\bar{G}}_{i,j+1}^{n+1} - \tilde{\bar{G}}_{i,j}^{n+1})] \quad (7d)$$

for the intersecting wedge grid points. Eq. (7a) remains unaltered.

At each step of the integration procedure, it is necessary to calculate the conservative variables $\bar{F}$ and $\bar{G}$ which are functions of the flow variables and the independent variables (ζ, η, ξ). The flow variables p, ρ, u, v, w are obtained by decoding the conservative variable $\bar{E}$. This necessitates the solution of the following five simultaneous, algebraic equations.

$$\begin{aligned} \bar{E}_1 &= r\zeta\rho u, \\ \bar{E}_2 &= r\zeta(kp + \rho u^2), \\ \bar{E}_3 &= r\zeta\rho uv, \\ \bar{E}_4 &= r\zeta\rho uw, \\ p &= \rho(1 - u^2 - v^2 - w^2). \end{aligned} \quad (8)$$

The solution of these equations is:

$$\begin{aligned} v &= \bar{E}_3/\bar{E}_1, \\ w &= \bar{E}_4/\bar{E}_1, \\ u &= \{-B + (B^2 - 4AC)^{1/2}\}/2A, \\ \rho &= \bar{E}_1/r\zeta u, \\ p &= \rho(1 - u^2 - v^2 - w^2), \end{aligned} \quad (9)$$

where $A = 1 - k$; $B = -\bar{E}_2/\bar{E}_1$; $C = k(1 - v^2 - w^2)$. The sign on the radical in the solution for u is taken to be positive for supersonic flows.

After the decoding procedure, the cross-flow velocities on the body surfaces are overwritten to satisfy the boundary conditions given by Eq. (5). Thus, with the free-stream conditions as the initial starting solution, Eq. (3) is integrated with respect to the marching direction ζ, and the flow variables are advanced from the initial data plane $\zeta = \zeta_0$ to $\zeta = \zeta_0 + \Delta\zeta$. At the beginning of each iteration cycle the current corrected flow variables are used at the initial data plane. The integration step size $(\Delta\zeta)$ is chosen to be the maximum possible value that yields a stable solution. As the iteration procedure converges the flow variables gradually approach their correct conical values.

V. Numerical Results

In this section the inviscid numerical solutions are compared with the experimental results of Charwat and Redekopp [1] and of Nangia [12]. Charwat and Redekopp performed their experiments for supersonic laminar flow over an

unswept axial corner at a Reynolds number of 2×10^6. Nangia obtained experimental results for supersonic flow over a swept axial corner including mixed compression–expansion. The flow was made artificially turbulent by tripping the boundary layer. In the comparisons that follow, a 30×30 rectangular grid was used for the numerical solutions and the computations were performed on an IBM 360/65 computer.

Case 1. $M_\infty = 3.17$; $\delta_B = 12.2^0$; $\delta_1 = 12.2°$; $\Lambda = 0°$. The computed shock and slip-surface structure is compared with the experimental results of Charwat and Redekopp in Fig. 7. The entire experimental wave structure is displaced

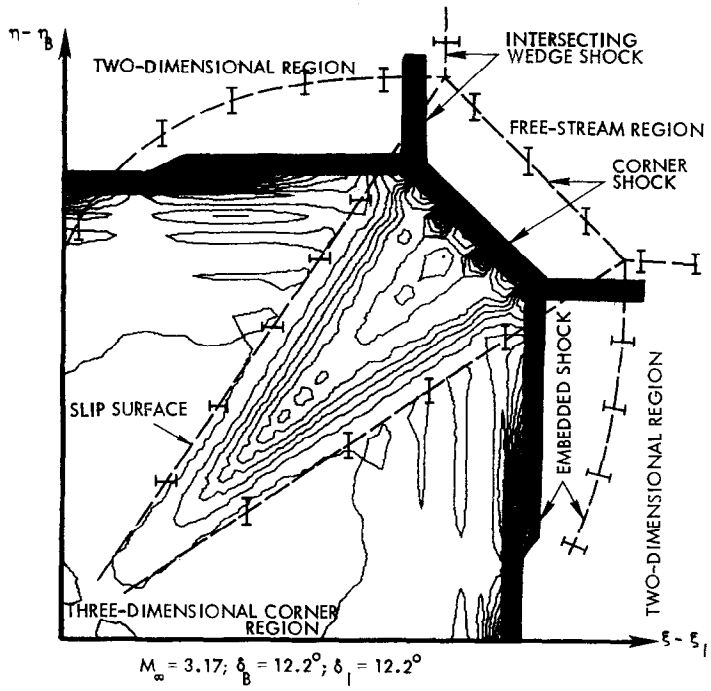

FIG. 7. Density contour plot in constant ζ computational plane (■ = Numerical results; I = Experimental results of Charwat and Redekeopp).

outward from that of the inviscid numerical results because of the effective thickening of the body due to the presence of a laminar boundary layer. The difference in the experimental data and the inviscid numerical results suggests that the viscous effects are more dominant in the three-dimensional corner region than in the two-dimensional wedge flow region. Contrary to the observations of

Charwat and Redekopp, no "outer zone of disturbance" is predicted in the region outboard of the embedded shock. The "outer zone of disturbance" observed by Charwat and Redekopp is probably due to the low Reynolds number laminar flow of their experiment. When viewed from the origin, the conical embedded shock is slightly concave. The slip surfaces are slightly curved and asymptotically approach the bisector near the axial corner. This is contrary to the straight slip surfaces indicated by Charwat and Redekopp.

A comparison of the numerical and experimental surface pressure distribution is shown in Fig. 8. The conical embedded shock is perpendicular to the wedge

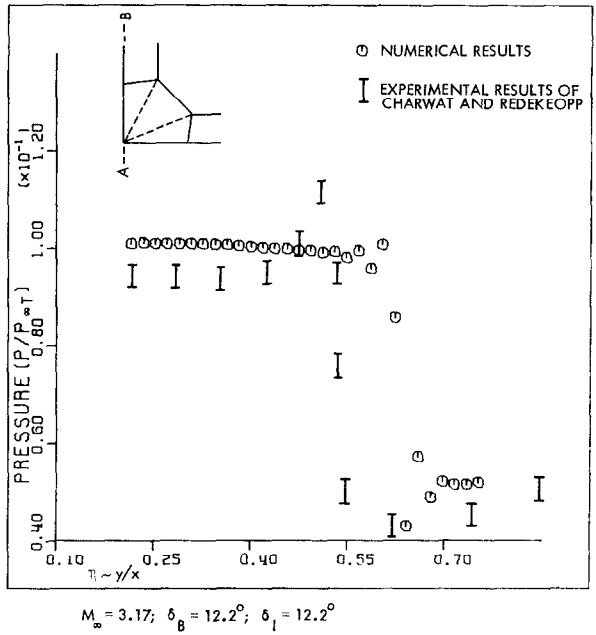

FIG. 8. Pressure distribution on the intersecting wedge surface.

surface at the impingement point in order to satisfy the surface tangency condition. The impingement location is marked by a rapid jump in pressure. The experimental impingement location is slightly inboard of the numerical prediction.

It required 512 iterations and 20 min of CPU time to obtain a converged solution with the free-stream conditions as the initial starting solution.

Case 2. $M_\infty = 2$; $\delta_B = 5°$; $\delta_I = 7.5°$; $\Lambda = 0°$. Nangia has obtained experimental results at Reynolds Number 3.0×10^6/ft for this asymmetric configuration. A numerical solution for the same case has been obtained, and the computed

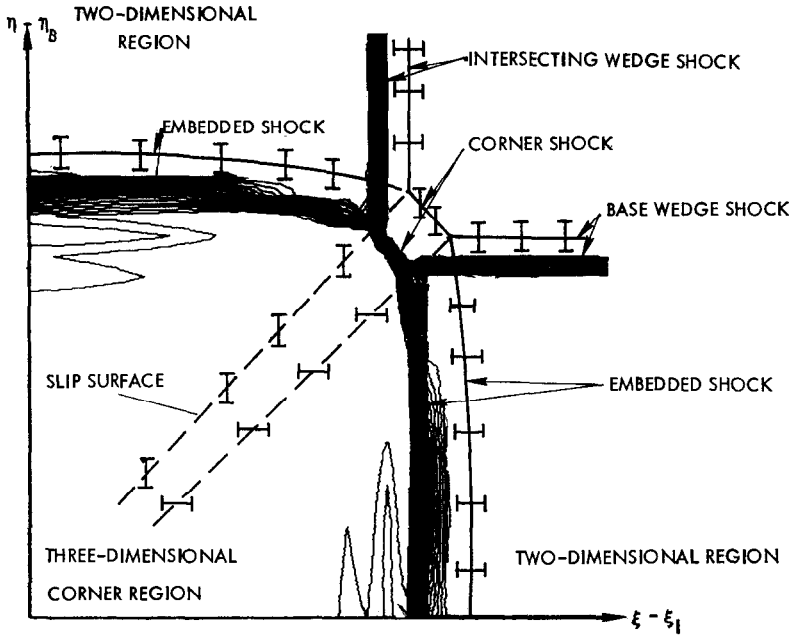

FIG. 9. Density contour plot in constant ζ computational plane (■ = Numerical results; = Experimental results of Nangia).

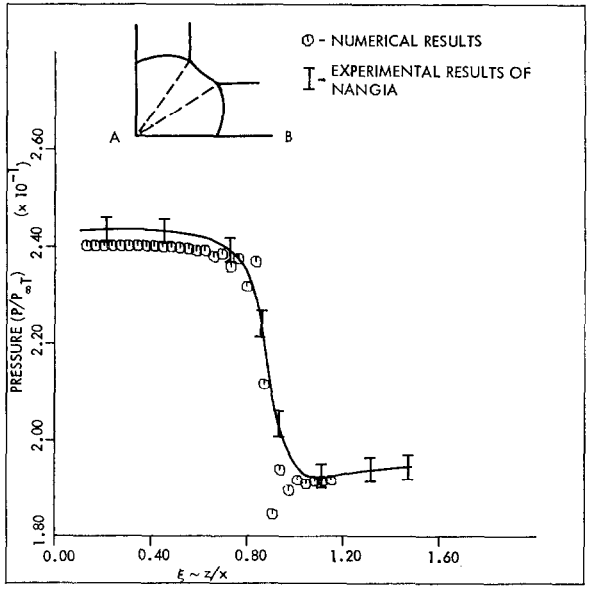

FIG. 10. Nondimensional pressure distribution on the base wedge surface.

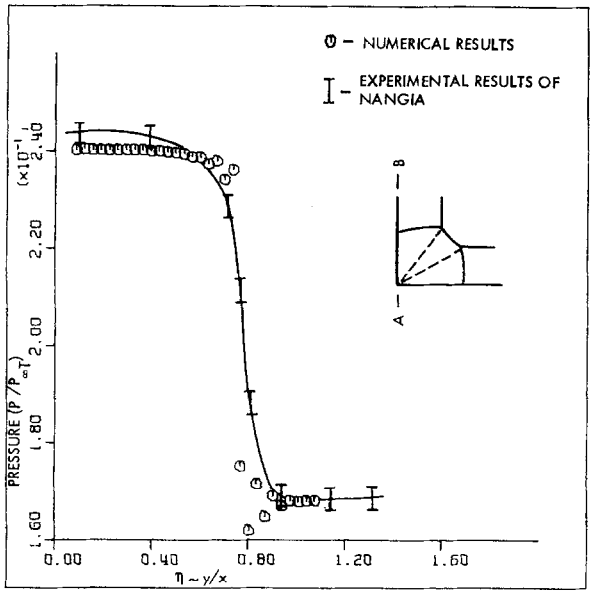

FIG. 11. Nondimensional pressure distribution on the intersecting wedge surface.

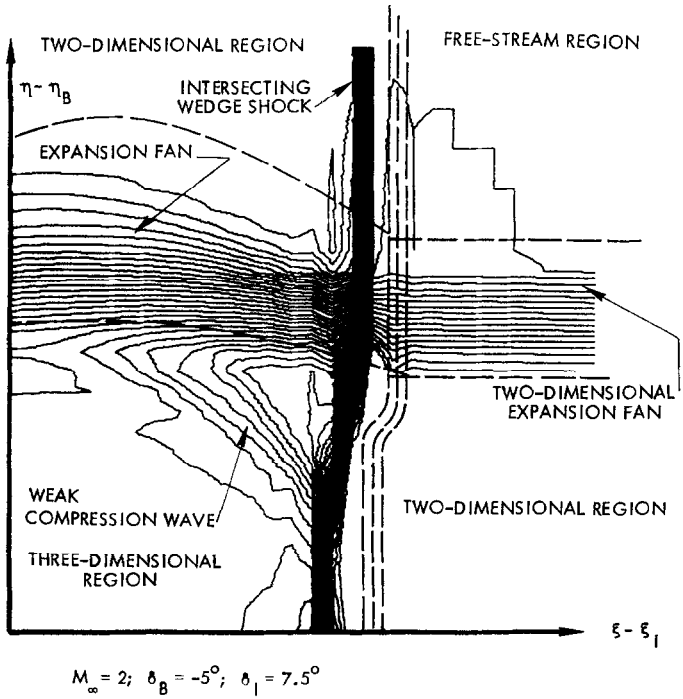

$M_\infty = 2$; $\delta_B = -5^\circ$; $\delta_I = 7.5^\circ$

FIG. 12. Pressure contour plot in constant ζ computational plane (■ = Numerical results; — — = Experimental results of Nangia).

inviscid shock structure is compared with the results of Nangia in Fig. 9. The effective thickening of the body for turbulent flow is considerably less than that for laminar flow in this problem, and as a result the inviscid numerical wave structure compares very well with the experimental prediction. When viewed from the origin, the horizontal and vertical embedded shocks are slightly concave while the corner shock is slightly convex.

The computed surface pressure distributions on the base and intersecting wedges are compared with the experimental results of Nangia in Figs. 10 and 11. In both cases the rapid rise in pressure (decreasing ξ and η) corresponds to the embedded shock impingement location.

The computation required 330 iterations and approximately 15 min of CPU time to obtain a converged solution.

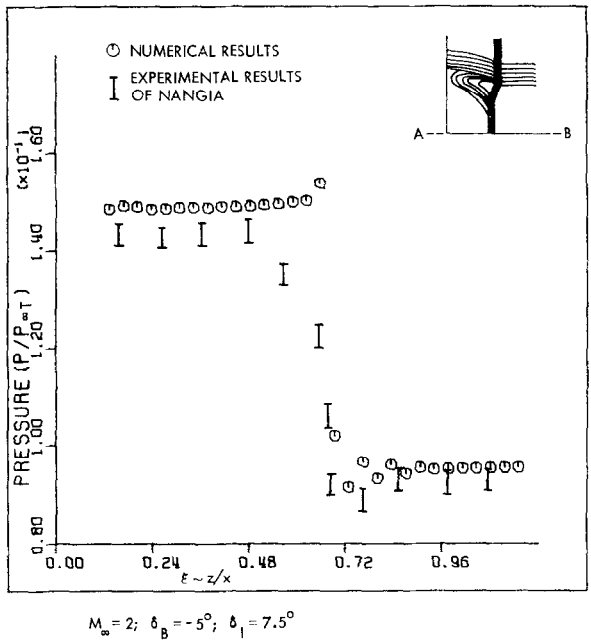

FIG. 13. Nondimensional pressure distribution on the base wedge surface.

Case 3. $M_\infty = 2$; $\delta_B = -5°$; $\delta_I = 7.5°$; $\Lambda = 0°$. The computed wave structure is compared with the experimental results of Nangia in Fig. 12 and shows very good agreement. It is interesting to note from Fig. 12 that the wave structure doesn't exhibit any corner shock or slip surfaces. This appears to be correct because changes through the expansion fan occur isentropically. However, an

auxiliary compression wave in the three-dimensional corner region is predicted by the numerical scheme which is not seen in the experimental results. The wedge expansion fan, after the interaction with the wedge shock, turns away from the axial corner and is concave when viewed from the origin, whereas the wedge shock turns toward the axial corner and appears to be slightly convex.

A comparison of the numerical and experimental nondimensional pressure distribution on the base wedge surface is shown in Fig. 13. The rapid change in the pressure marks the embedded shock impingement location. The strength of the shock at the impingement point is slightly more than that of the intersecting wedge shock. This is due to merging of the weak compression wave.

The computed pressure distribution on the intersecting wedge surface is compared with the experimental results of Nangia in Fig. 14. The gradual drop (decreasing η) in the pressure corresponds to the expansion fan, and the changes occur isentropically.

It required 218 iterations and approximately 10 min of CPU time to obtain a converged solution.

Case 4. $M_\infty = 2$; $\delta_B = 5°$; $\delta_I = 7.5°$; $\Lambda = 30°$. Nangia [12] has obtained experimental (turbulent boundary layer) results at Reynolds number 3.0×10^6/ft for this corner configuration. A numerical solution for the same case is obtained,

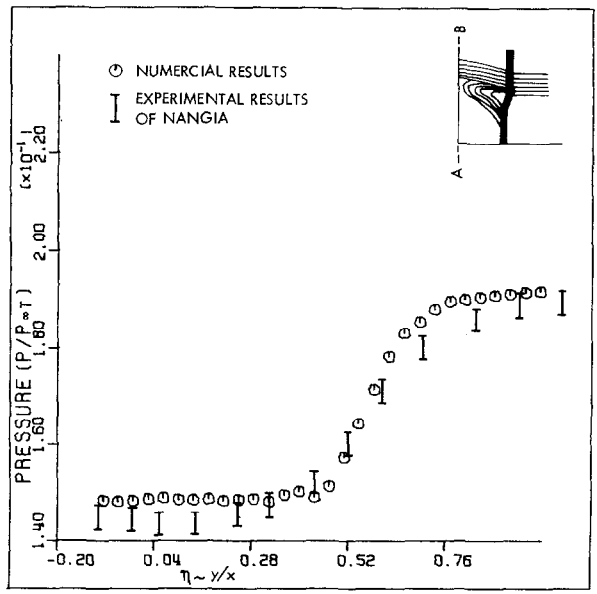

FIG. 14. Nondimensional pressure distribution on the intersecting wedge surface.

and the computed inviscid shock structure is compared with the results of Nangia in Fig. 15. The swept-base wedge shock and the intersecting wedge shock are joined by a third corner shock, with embedded shocks bounding the corner region. The flow structure is similar to unswept compression–compression corner results. The embedded shock from the upper triple point is concave when viewed from the origin and turns away from the axial corner, whereas the embedded shock from the lower triple point is straight. A set of compression fans originate

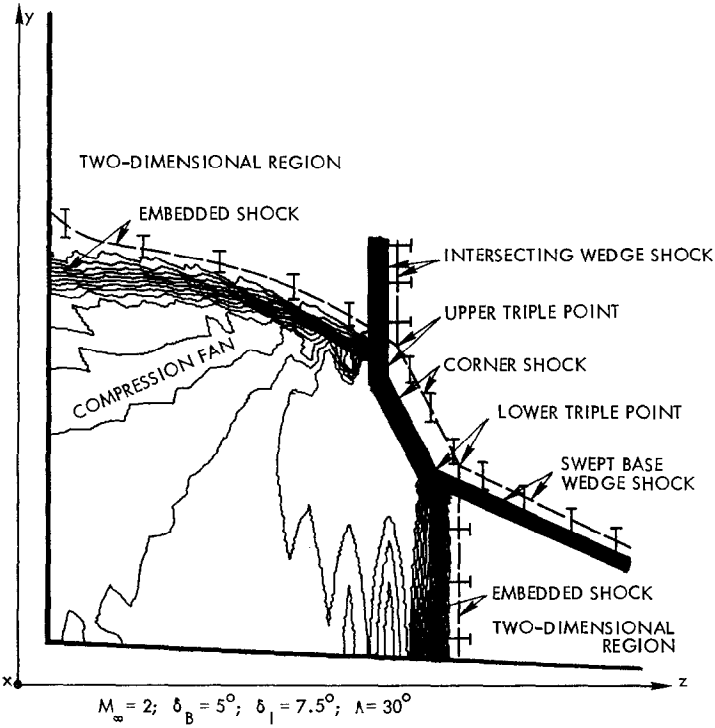

FIG. 15. Pressure contour plot in constant x physical plane (■ = Numerical results; I = Experimental results of Nangia).

at the upper triple point and spread over the entire three-dimensional corner region. The wave structure indicates no presence of slip surfaces although one expects them to be present.

Figures 16 and 17 show the computed surface pressure distribution on the base and intersecting wedges compared with the experimental results of Nangia. In Fig. 17 the first sharp jump (decreasing η) corresponds to the curved horizontal embedded shock. This jump is followed by a gradual rise in pressure across the

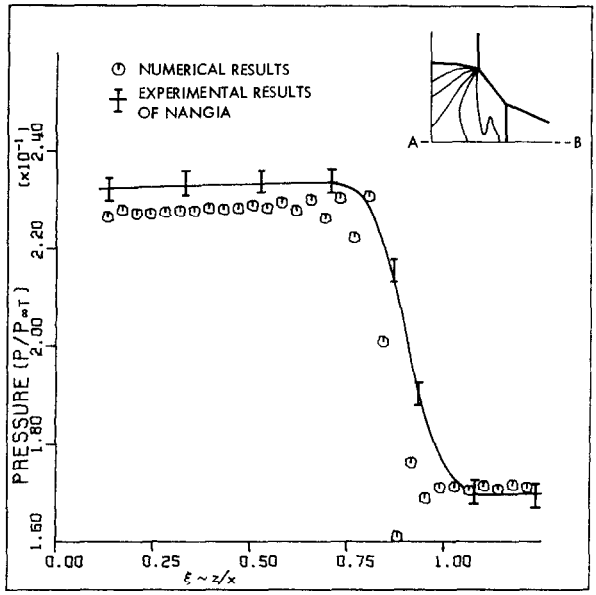

$M_\infty = 2;\ \delta_B = 5^\circ;\ \delta_1 = 7.5^\circ;\ \Lambda = 30^\circ$

FIG. 16. Nondimensional pressure distribution on the swept base wedge surface.

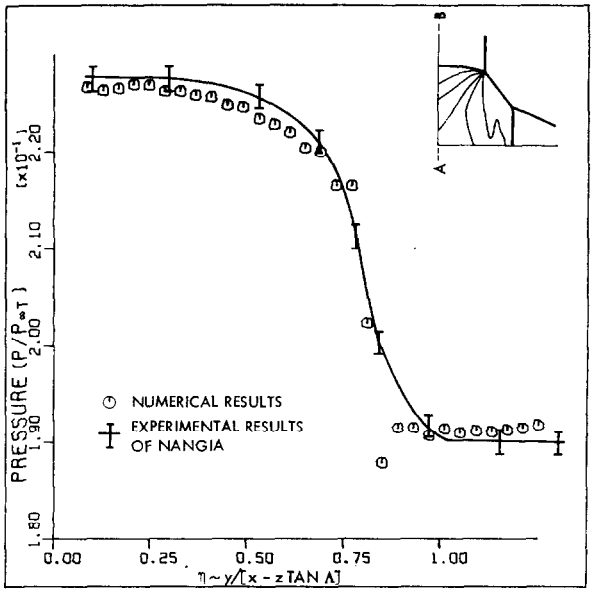

$M_\infty = 2;\ \delta_B = 5^\circ;\ \delta_1 = 7.5^\circ;\ \Lambda = 30^\circ$

FIG. 17. Nondimensional pressure distribution on the intersecting wedge surface.

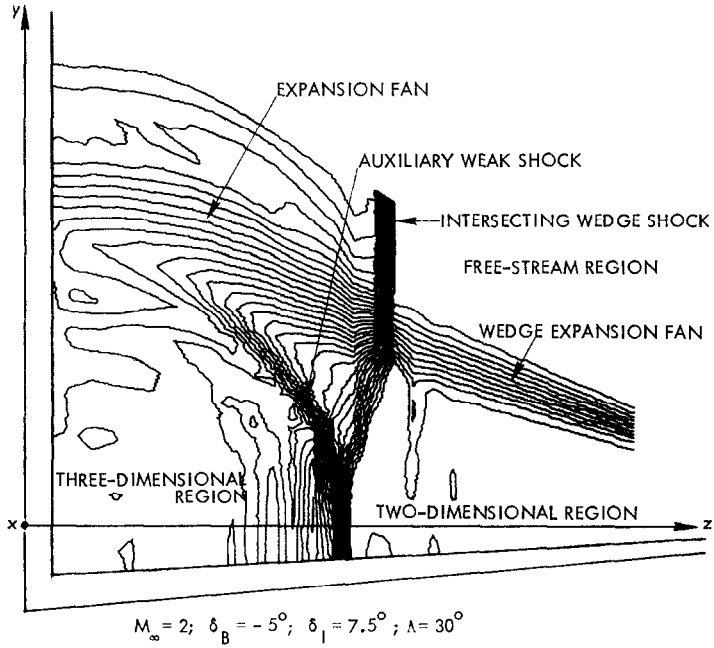

FIG. 18. Pressure contour plot in constant x physical plane.

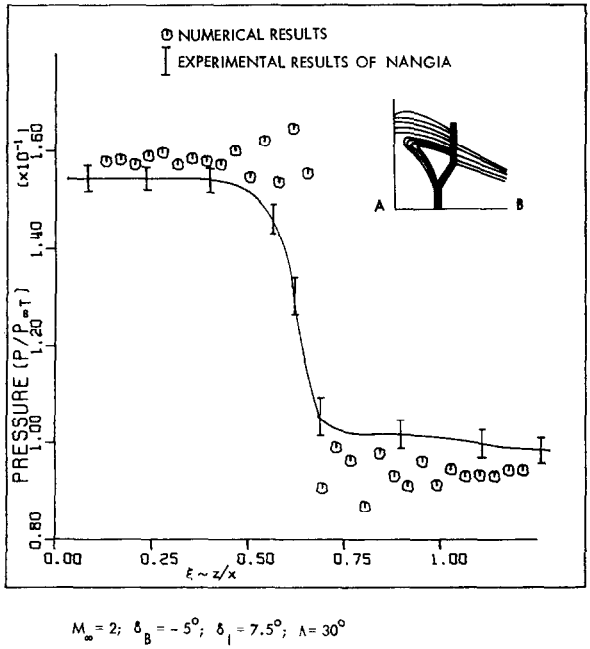

$M_\infty = 2;\ \delta_B = -5^\circ;\ \delta_I = 7.5^\circ;\ \Lambda = 30^\circ$

FIG. 19. Nondimensional pressure distribution on the swept base wedge surface.

compression fan. The horizontal embedded shock is weak compared to the vertical embedded shock.

It required 740 iterations and approximately 30 min of CPU time to obtain a converged solution.

Case 5. $M_\infty = 2$; $\delta_B = -5°$; $\delta_I = 7.5°$; $\Lambda = 30°$. The pressure contour plot shown in Fig. 18 illustrates the computed wave structure in the corner. The wedge expansion fan, after interacting with the wedge shock, turns away from the axial corner and appears to be concave when viewed from the origin. The intersecting wedge shock is deflected towards the axial corner under the influence of the wedge expansion fan. An auxiliary weak shock is formed in the three-dimensional corner

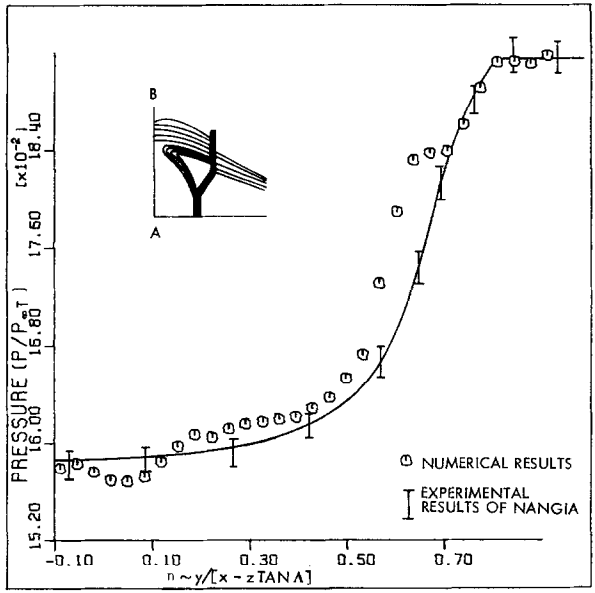

FIG. 20. Nondimensional pressure distribution on the intersecting wedge surface.

region which merges with the weak embedded shock and forms a strong shock near the base wedge surface. The shock impingement on the base wedge surface is nearer the axial corner than the wedge shock. The strength of the impinging shock appears to increase with increasing sweep angle. Furthermore, the interference region decreases as the sweep angle increases.

The computed pressure distribution on the base and intersecting wedge surfaces are compared with the experimental results of Nangia in Figs. 19 and 20. It required 552 iterations to obtain a converged solution for this case.

VI. Concluding Remarks

The problem of swept axial corner flow has been treated. This required the development of a coordinate transformation which conveniently mapped the physical coordinate system into a suitable computational system including sweep. Corner flows including both compression and expansion surfaces were treated in this system.

Use of the shock-capturing technique provided an accurate description of the wave structure for an otherwise complicated interference flow problem. The inviscid numerical results indicate that the wave structure in the corner at relatively high Reynolds numbers is determined by the inviscid flow field and the viscous effects result only in an effective thickening of the body which forces the wave structure outwards. When the boundary layer is laminar, the effective thickening of the body is more dominant than when the boundary layer is turbulent. Thus, inviscid numerical solutions agree more favorably with the experimental results for the turbulent case than for the laminar case. Numerical solutions to viscous corner flows at relatively high Reynolds numbers can be obtained by an inviscid analysis of the problem after suitably superimposing the effect of the boundary layer by incorporating it in the body thickness.

Numerous extensions of the present work suggest themselves. A significant class of problems remain to be solved using the techniques discussed in the present paper. The most obvious problem is the solution of corner flows in which the wedge intersection does not form a 90° corner. This is in essence a sort of dihedral for obtuse angles. Perhaps of more interest is the problem of solving swept corner flow when the shock produced by the intersecting wedge lies outside of the leading edge of the base wedge. This is an off-design condition and is of considerable practical importance in supersonic inlet systems. A number of other extensions could be based upon the present analysis including flow over external corners.

Acknowledgment

This work was sponsored by NASA under NASA-Ames/University Aerospace Institutes agreement, ISU-301 through the Iowa State Engineering Research Institute. The authors wish to acknowledge the encouragement given to them throughout this investigation by Dr. Paol Kutler.

REFERENCES

1. A. F. CHARWAT AND L. G. REDEKOPP, *AIAA J.* **5** (1967), 480–488.
2. R. H. KORKEGI, "A Limiting Condition for Supersonic Inviscid Interaction in the Corner of Intersecting Wedges," ARL 68–0099, 1968.
3. R. D. WATSON AND L. M. WEINSTEIN, *AIAA J.* **9** (1971), 1280–1286.
4. R. J. CRESCI *et al.*, *AIAA J.* 7 (1969), 2241–2246; see also Papers 14 and 18, AGARD Conference Proceedings No. 30, May 1968.
5. P. C. STAINBACK, "Heat Transfer Measurements at a Mach Number of 8 in the Vicinity of a 90° Interior Corner Aligned with the Free-Stream Velocity," TN D-2417, 1964, NASA.
6. P. C. STAINBACK, "An Experimental Investigation at a Mach Number of 4.95 of Flow in the Vicinity of a 90° Interior Corner Aligned with the Free-Stream Velocity," TN D-184, 1960, NASA.
7. MAJOR J. E. WEST AND R. H. KORKEGI, "Interaction in the Corner of Intersecting Wedges at a Mach Number of 3 and High Reynolds Numbers," ARL 71-0241, 1971.
8. J. WALLACE AND J. H. CLARKE, *AIAA J.* **1** (1963), 179–185.
9. T. P. GOEBEL, A Theoretical Study of Inviscid Supersonic Flow Along a Corner Formed by the Intersection of Two Wedges, Ph.D. Thesis, Univ. of California, Los Angeles, 1969.
10. R. H. KORKEGI, *AIAA J.* **9** (1971), 771–783.
11. P. KUTLER, *AIAA J.* **12** (1974), 577–578.
12. R. K. NANGIA, "Three-Dimensional Wave Interactions in Supersonic Intakes," Second International Symposium on Air Breathing Engines, 25th–29th March, 1974, Sheffield, U.K.
13. R. W. MACCORMACK, "The Effect of Viscosity in Hypervelocity Impact Cratering," AIAA Paper 69-35A, 1969.